PCCP

Accepted Manuscript

ROYAL SOCIETY OF CHEMISTRY

www.rsc.org/pccp

Journal Name

RSCPublishing

ARTICLE

A theoretical modeling of the $L_{2,3}$-edge X-ray absorption spectra of $Mn(acac)_2$ and $Co(acac)_2$ complexes.†‡

Cite this: DOI: 10.1039/x0xx00000x

Received 00th January 2012,
Accepted 00th January 2012

DOI: 10.1039/x0xx00000x

www.rsc.org/

Silvia Carlotto,[*a] Mauro Sambi,[a] Andrea Vittadini[b] and Maurizio Casarin[*a,b]

$Mn(acac)_2$ (**I**) and $Co(acac)_2$ (**II**) $L_{2,3}$-edge absorption spectra have been modeled by using the DFT/ROCIS method. Besides the agreement between experiment and theory, the combined use of the B3LYP exchange-correlation functional and of the def2-TZVP(-f) basis set provided useful information about the coordinative geometry around the M(II) ions as well as about the nature and the strength of the Mn–O and Co–O interaction. The lower excitation energy (*EE*) side of both $^{\mathbf{I/II}}L_3$ and $^{\mathbf{I/II}}L_2$ intensity distributions mainly includes states having the ground state spin multiplicity (S = 5/2 in **I**; S = 3/2 in **II**), while states with lower spin multiplicity (S = 3/2 in **I**; S =1/2 in **II**) significantly contribute to the higher *EE* side of both $^{\mathbf{I/II}}L_3$ and $^{\mathbf{I/II}}L_2$. As such, the occurrence on L_3 and L_2 higher *EE* sides of states involving metal to ligand charge transfer transitions in the presence of ligands with low lying empty π* orbitals is herein confirmed.

1. Introduction

X-Ray Absorption Spectroscopy (XAS) of M complexes (M = metal of the first transition series) is a powerful tool able to provide useful information about low lying virtual orbitals, the M geometrical environment, the nature and the strength of the M-ligand bonding.[1-3] The XAS versatility has been extensively exploited to investigate highly different chemical systems including single molecules,[3-4] solids,[5] minerals[6] and metalloproteins.[7] Inasmuch as XAS features are associated to the excitation of core electrons to the frontier unoccupied molecular orbitals (MOs) as well as to the continuum, K- and L-edge[8] spectra are very sensitive to both the electronic structure and the local surrounding of the absorbing atom. As such, M K-edge spectral structures are generated by the electric dipole forbidden, but quadrupole allowed, $1s^M \rightarrow n d^M$ transitions,[9-11] which may be enhanced in non-centro-symmetric complexes through the involvement of $(n + 1)p^M$ atomic orbitals (AOs) into frontier unoccupied MOs.[12-13] At variance to that, the potentially richer M $L_{2,3}$-edge structures are dominated by the electric dipole allowed $2p^M \rightarrow n d^M$ transitions,[9,14] thus probing the contribution of $n d^M$ AOs to the unoccupied electronic structure. The $2p^6 \rightarrow n d^k$ transitions produce a final electronic configuration with a hole in the $2p^M$ core levels ($2p^5 n d^{k+1}$) whose orbital angular momentum is ℓ = 1; this will couple to the spin angular momentum s = 1/2 to generate j = 3/2 and j = 1/2 states as a consequence of the spin-orbit coupling (SOC). The former state (j = 3/2) lies at lower excitation energy (*EE*) and it corresponds to the L_3 feature,[8] whose intensity is approximately twice the one of the L_2 feature[8] associated to the j = 1/2 state.[15-16] Both the experimental analysis and the theoretical modeling of $L_{2,3}$-edge spectra in M complexes are challenging issues; in fact, besides ligand-field and covalency effects, the SOC between the possibly many final-state multiplets has to be taken into account.[4-5,17-19]

$Mn(acac)_2$ and $Co(acac)_2$ (hereafter, **I** and **II**, respectively; acac = 2,4-pentanedionato) are the only *tetrahedral* M complexes of the (bis-acac)$^{2-}$ ligand.[20] In fact, $V(acac)_2$ has a distorted square pyramidal coordination environment; the bis-acac O atoms of $VO(acac)_2$ generate the equatorial plane of a square pyramid whose apex is occupied by the vanadyl oxygen;[19e,24] Cr(II) lies on an inversion center and has a planar coordination by four oxygen atoms in $Cr(acac)_2$;[25] $Fe(acac)_2$, quickly converted into $Fe(acac)_3$ in solution under aerobic conditions, crystallizes as a tetramer[26] with "two O-bridged dinuclear units that are further held together by a rather long Fe–C bond between the inner Fe atom of one unit with one acetylacetonate central C atom of the adjacent one";[27] anhydrous $Ni(acac)_2$ is trimeric ($Ni_3(acac)_6$) with an octahedral

[a] Dr. Silvia Carlotto, Prof. Mauro Sambi, Prof. Maurizio Casarin Dipartimento di Scienze Chimiche, Università degli Studi di Padova, Via F. Marzolo 1 - 35131 Padova, Italy
E-mail: maurizio.casarin@unipd.it, silvia.carlotto@unipd.it
[b] Dr. Andrea Vittadini, Prof. Maurizio Casarin Istituto per l'Energetica e le Interfasi, IENI-CNR via Marzolo 1, 35131 Padova, Italy

coordination around each Ni(II) ion;[28-30] finally, $Cu(acac)_2$ has a square planar arrangement.[31]

Manganese complexes have been extensively investigated with $L_{2,3}$-edge XAS investigations[32-38] because of their diverse technological applications, which include magnetic semiconductors for spintronic materials,[32-34] battery electrodes,[35] ferrimagnetic nanoparticles for magnetic recording media and transformers,[36] thin films[37] up to biological applications.[38] Similarly to Mn, Co complexes have been exploited for a massive number of applications, which again include magnetic semiconductors for spintronic materials,[39] ferrimagnetic nanoparticles for magnetic recording media and transformers,[36] catalysts[40] and nanocrystals for catalytic reactions.[41] It is not then surprising that, likely to Mn, $L_{2,3}$-edge XAS has been extensively employed to investigate Co-based materials.[36,39-41]

The $L_{2,3}$-edge XA spectrum of **I** has been firstly reported by Grush *et al.*[42] in an experimental study of Mn complexes,[43] while Collison *et al.*[44] used the $L_{2,3}$-edge XA spectrum of **II** to gauge the spectrum of the $Co(acac)_3$ photoreduction products. In none of these contributions the $^{\mathbf{I/II}}L_{2,3}$-edge XA features were analyzed in detail. In the present study, literature[42,44] $^{\mathbf{I/II}}L_{2,3}$-edge XA spectra have been modeled by adopting the recently developed Restricted Open shell Configuration Interaction with Singles (hereafter, DFT/ROCIS) method.[19d] The origin of the fine multiplet spectral features is thoroughly discussed and analyzed from both a qualitative and quantitative point of view. Moreover, the peculiar M role on spectral shapes and feature positions are considered in detail.

2. Computational Details

All the calculations have been performed by employing the ORCA program package.[45] Molecular geometry optimizations[46] have been carried out by adopting the hybrid Becke3−Lee−Yang−Parr (B3LYP)[47] exchange-correlation functional, i.e., by combining a standard generalized gradient (VWNIII) with a part (20%) of Hartree−Fock exchange, and by using the def2-TZVP(-f) basis set.[48-49] $L_{2,3}$ *EE*s, transition dipole moments and their intensities have been evaluated by means of the DFT/ROCIS method,[17,19d,50] which includes SOC in a molecular Russell-Saunders fashion. As a consequence of the strong 2p SOC in the final state manifold, excited states with spin quantum numbers (S) different from that of the ground state (GS) have had to be computed. The combined use of DFT and CI requires a set of three semi-empirical parameters (c_1 = 0.18, c_2 = 0.20, and c_3 = 0.40),[19d] which have been calibrated by Roemelt and Neese[17] for a test set of ^{M}L-edges. Saturation of the final-state manifold has been obtained by considering forty nonrelativistic roots per multiplicity. Throughout the numerical experiments, the resolution of identity (RI) approximation[51] has been used with the def2-TZVP/J basis set.[48b] Moreover, the zeroth order regular approximation has been adopted to treat the scalar relativistic effects.[52] Numerical integrations for all the calculations have been carried out on a dense Lebedev grid (302 points).[53] Simulated spectra have been shifted by 13.4 eV in **I** and 14.2 eV in **II** to superimpose the highest intensity feature of the experimental and simulated L_3 spectra, which do not suffer of extra broadening and distortion due to the Coster-Kronig Auger decay process.[4,54] Incidentally, this is needed because absolute theoretical *EE*s carry errors arising from DF deficiencies in the core region, one-particle basis set restrictions and inadequacies in the modeling of spin-free relativistic effects.[4] A Gaussian broadening factor of 0.8 eV has been throughout applied to model $^{\mathbf{I/II}}L_{2,3}$-edge XA spectra.

3. Results and discussion

$Co(acac)_2$ presents interesting features, as it can take two spin states, viz. a low-spin (LS) doublet or a high-spin (HS) quartet,[55-56] and three structural arrangements, i.e., square-planar, tetrahedral or octahedral with two coordinative positions occupied by solvent molecules.[57-58] Early experiments carried out by the Cotton group seemed to be consistent with a Co(II) tetrahedral environment[59] and a HS GS.[60] This has been recently confirmed by the complete active space self-consistent field/second-order perturbation theory (CASSCF/CASPT2)[55] and DFT[21,56,61] calculations. Unlike **II**, neither the molecular structure nor the GS spin state of **I** have raised interest in literature.[62] As such, Grush *et al.*[42-43] suggested quite apodictically a tetrahedral geometry for **I**. To look into such an assumption, different Mn(II) coordinative environments (distorted tetrahedral and square-planar) and spin multiplicities (S = 5/2 for the distorted tetrahedral coordination; S = 5/2 and S = 3/2 for the square planar one) have been herein considered with the following outcomes: the B3LYP GS energy associated to the square planar coordinative arrangement with S = 5/2 (S = 3/2) is higher than that corresponding to the HS distorted tetrahedral structure (see Figure 1) by 7.9 (17.0) kcal/mol.[64] Different Mn(II) coordinative arrangements are compared in the Figure S1 of the ESI.

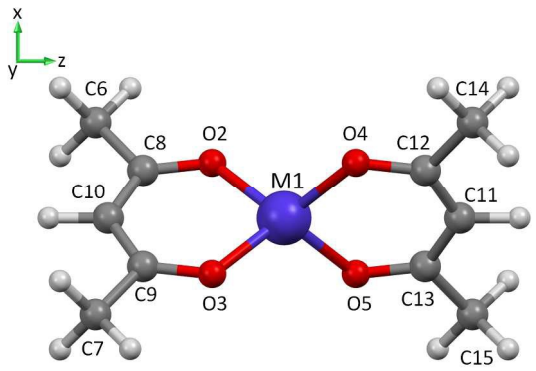

Figure 1. Schematic representation of $M(acac)_2$, M = Mn (**I**) and Co (**II**). Violet, red, grey and white spheres correspond to the M, O, C and H atoms, respectively.

Optimized geometries (see Tables S1 and S4 of ESI) indicate that, on passing from **I** to **II**, the M–O bond length decreases less than 5% (2.04 vs 1.95 Å). In this regard, it is worth of note that the optimized Co-O inter-nuclear distance is

quite close to the ones (1.94 – 2.00 Å) evaluated by Radon *et al.*[55] in their DFT calculations, where a number of functionals and basis sets were considered. It is also noteworthy that, both in **I** and **II**, optimized geometries significantly deviate from a regular tetrahedral environment of the M center. As such, the O4–M1–O5 angle is sharper in **I** (89.9°) than in **II** (95.7°) and, as the Co–O bond length, the O4–Co–O5 angle is very similar to that estimated by other DFT studies (97.4° and 97.7°).[56] As far as the O2-M1-O4 angle is concerned, we find it to be wider in **I** (120.1°) than in **II** (116.8°). Now, before entering into the details of the obtained theoretical results, a preliminary description of the nature of the main 2p → 3d one-electron excitations, carried out in the habit of a ligand field theory type of analysis (see Figure 2), coupled to a qualitative picture, simply based on symmetry arguments, of the acac$^-$/(bis-acac)$^{2-}$ frontier MOs may be useful to favor the comprehension of the forthcoming discussion.

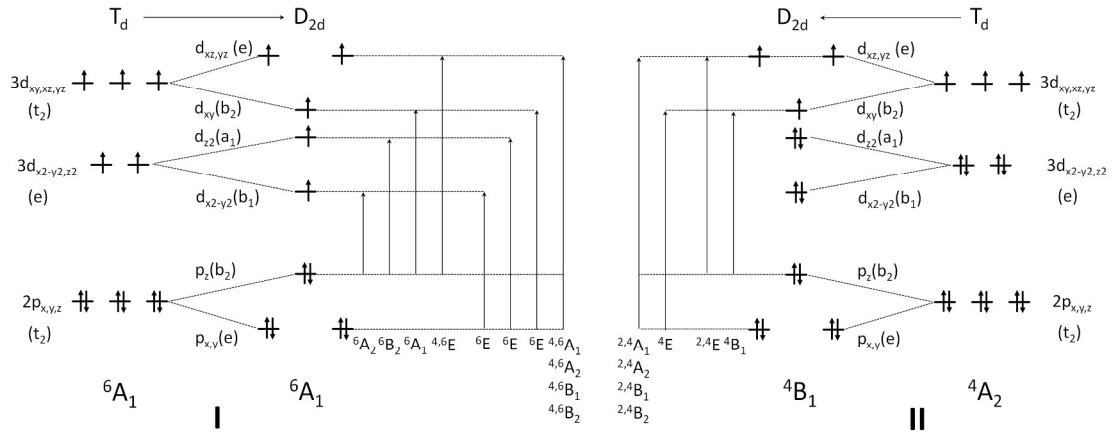

Figure 2. MO splitting diagram of **I** and **II** within the assumption of a regular/distorted tetrahedral arrangement around M. Adapted 2p → 3d transitions in the one-electron particle/hole approximation are also displayed. HS orbital occupation patterns refer to the $^6A_1$ (**I**) and $^4B_1$ (**II**) ground states.

The occupation numbers of 3d AOs in Mn(II) and Co(II) free ions are five ($3d^5$, GS = ^{6}S) and seven ($3d^7$, GS = ^{4}F), respectively. Upon a 2p → 3d one-electron excitation, the M final electronic configuration is then $2p^53d^6$ in Mn(II) and $2p^53d^8$ in Co(II).[65] If the whole set of multiplets arising from the $3d^6$ ($3d^8$) configuration is collectively labeled as ^{6}D (^{8}D), the electronic states generated by the $2p^53d^6$ ($2p^53d^8$) configuration are:[65-66] $^2P \otimes {}^6D = {}^{2,4}S, {}^{2,4,6}P, {}^{2,4,6}D, {}^{2,4,6}F, {}^{2,4}G, {}^{2,4}H, {}^{2,4}I, {}^2K$ ($^2P \otimes {}^8D = {}^{2,4}S, {}^{2,4}P, {}^{2,4}D, {}^{2,4}F, {}^{2,4}G, {}^2H$). As a consequence of the ligand field, covalent interactions and SOC admixture, these states will further split to generate a total of 6 × 210 = 1260 (6 × 45 = 270) molecular magnetic spin sublevels with $M_S = \pm1/2, \pm3/2, \pm5/2$ ($M_S = \pm1/2, \pm3/2$). According to Maganas *et al.*,[4] they have been labeled |±1/2>, |±3/2> and |±5/2>. The one electron excitation pattern describing the M final states in the tetrahedrally distorted structure (D_{2d} symmetry point group) of **I** and **II** is then dominated by states having either a spin multiplicity equal (ΔS = 0) or lower (ΔS = –1) than the GS one (S = 5/2 in **I**, S = 3/2 in **II**) (see Figure 2).[67-68] The forthcoming analysis of $^{\mathbf{I/II}}L_{2,3}$-edge spectra will be then carried out by treating explicitly these excitation patterns in the habit of an appropriate CI scheme, which includes electron correlation and anisotropic covalency.

The acac$^-$/(bis-acac)$^{2-}$ frontier MOs may be factored in two sets according to their σ or π character.[69] The σ set consists of two completely occupied orbitals: the in-phase (n_+) and the out-of-phase (n_-) linear combinations of the O lone-pairs, both of them lying in the acac$^-$ plane. The latter set consists of five π orbitals (π_i, i = 1 - 5), three of them (π_j, j = 1 - 3) completely occupied. As far as the empty π MOs are concerned, both π_4 and π_5 are C–O antibonding; moreover, π_4 has a node on the methinic carbon atom [C(H)], while π_5 is also C–C(H) antibonding. When the (bis-acac)$^{2-}$ ligand is considered, each σ and π acac-based frontier MO generates in-phase (σ^+/π^+) and out-of-phase (σ^-/π^-) combinations; $n_+^+, n_+^-, n_-^+, n_-^-$ transform as the a_1, b_2 and e irreducible representations (IRs) of the D_{2d} symmetry point group, while $\pi_1^+, \pi_1^-, \pi_2^+, \pi_2^-, \pi_3^+, \pi_3^-, \pi_4^+, \pi_4^-, \pi_5^+, \pi_5^-$ belong to the e, a_2, b_1, e, a_2, b_1, e IRs, respectively.

The actual relative positions of the frontier MOs of **I** together with dominant one-electron 2p → 3d excitations are displayed in Figure 3 (HOMO – LUMO ΔE = 4.53 eV).[70] In agreement with qualitative predictions, the $^{\mathbf{I}}$GS is a $^6A_1$; nevertheless, it is noteworthy that this state is generated by an electronic configuration completely different from that reported in Figure 2. More specifically, among the five Mn(II) 3d-based MOs, two of them (the t_2-like *xy* and the e-like $x^2 - y^2$) are fulfilled (DOMO),[71] while the latter e-like (z^2) and the remaining two t_2-like (*xz*/*yz*) correspond to SOMOs (see Figure 3).[71] As far as the left over two unpaired electrons are concerned, they occupy a double degenerate, (bis-acac)$^{2-}$–based MO (the corresponding atomic character is reported in Table S5 of the ESI together more detailed 3D contour plots), characterized by the symmetry allowed contribution of both n_-^+, n_-^- and π_3^+, π_3^- pairs (both of them transforming as the e IR) and lying in between the z^2 HOMO-2 and the *xz*/*yz* HOMO. Upon closer inspection, the HOMO and the HOMO-1 appear to correspond to the anti-bonding and non-bonding combinations

between the Mn(II) t_2-like *xz*/*yz* AOs and the just described $(bis\text{-}acac)^{2-}$–based hybrid orbital.[72]

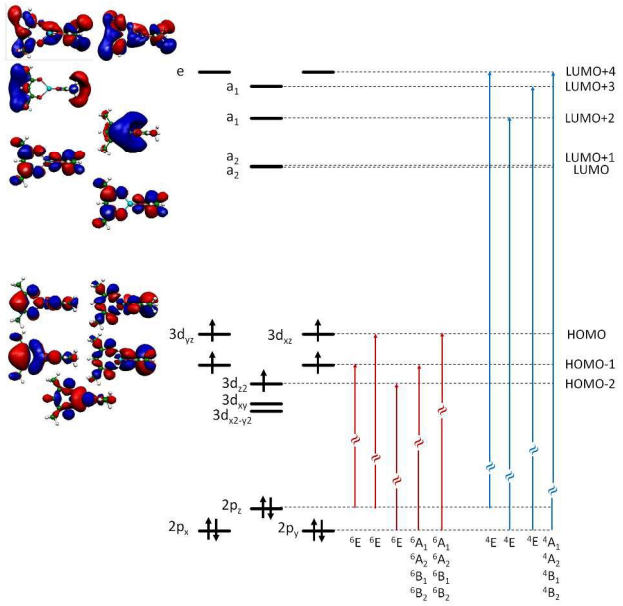

Figure 3. Dominant contributions to the L_3-edge spectrum of **I**. The HS orbital occupation pattern refers to a $^6A_1$ ground state. In the adopted framework, the Mn 3d-based AOs transform as a_1 (z^2); b_1 ($x^2 - y^2$); b_2 (*xy*); e (*xz*, *yz*), while the Mn 2p AOs transform as b_2 (*z*); e (*x*, *y*). Both the 3d($x^2 - y^2$) and the 3d(*xy*) are DOMOs, the absence of any arrow on them is for the sake of clarity.

The actual relative positions of frontier MOs in **II** (see Figure 4, HOMO – LUMO ΔE = 4.96 eV) look like similar to the ones displayed in Figure 3 for **I**,[70] the main unlikeness being the different number of electrons contributed by Co(II), which fulfill the e-like z^2 HOMO-2[73] and leave a single hole in the HOMO-1. Incidentally, such an electronic configuration generates a GS (^4E)[74] different from that foreseen on a qualitative ground ($^4B_1$, see Figure 2).

Besides these macroscopic differences, a thorough analysis of B3LYP GS ORCA[45] results underlies a M–ligand interaction stronger in **II** than in **I**. As a matter of fact, i) the contribution of the M 3d-based t_2-like *xz*/*yz* AOs to the bonding combination with the $n_-^+, n_-^- / \pi_3^+, \pi_3^-$ $(bis\text{-}acac)^{2-}$-based hybrid is slightly larger in the HOMO-6 of **II** (45%) than in the HOMO-6 of **I** (43%) (see Table S5 and S6 of the ESI);[72] ii) the contribution of M 3d-based t_2-like *xz*/*yz* AOs to the anti-bonding combination with the $n_-^+, n_-^- / \pi_3^+, \pi_3^-$ $(bis\text{-}acac)^{2-}$-based hybrid is significantly smaller in the HOMO of **II** (12%) than in the HOMO of **I** (25%); iii) the overall M–O overlap population is smaller in **I** (0.28*e*) than in **II** (0.33*e*) and accordingly iv) the M–O bond distance is shorter in **II** (1.95 Å) than in **I** (2.04 Å); finally, v) the M Mulliken gross atomic charge[76] is larger in **I** (0.97*e*) than in **II** (0.76*e*), thus suggesting a higher ionic contribution to the Mn–O interaction when compared to the Co–O one.

XAS spectra. It has been already emphasized that neither the molecular structure of **I** nor its GS spin state have been extensively debated in literature.

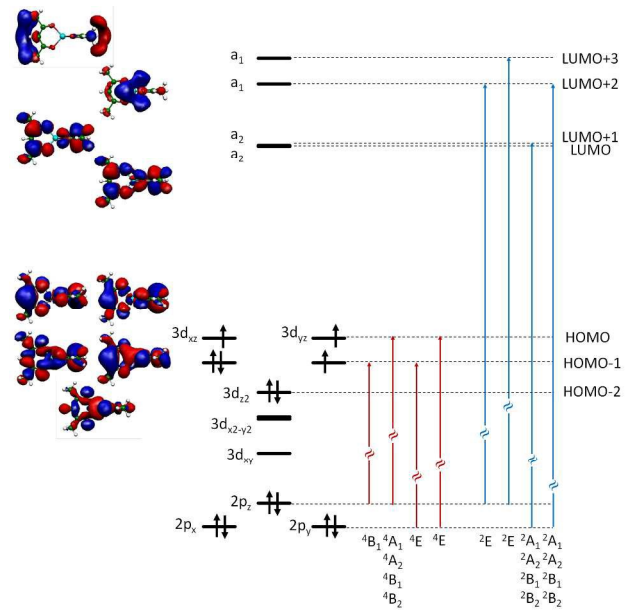

Figure 4. Dominant contributions to the L_3-edge spectrum of **II**. The HS orbital occupation pattern refers to a $^4B_1$ ground state. In the adopted framework, the Co 3d-based AOs transform as a_1 (z^2); b_1 ($x^2 - y^2$); b_2 (*xy*); e (*xz*, *yz*), while the Co 2p AOs transform as b_2 (*z*); e (*x*, *y*). Both the 3d(*xy*) and the 3d($x^2 - y^2$) are DOMOs, the absence of any arrow on them is for the sake of clarity.

In this regard, the $^1L_{2,3}$-edge XA spectrum (see Figure 5(a)) has been analyzed by Grush *et al*.[42-43] on the basis of a postulated HS tetrahedral geometry.

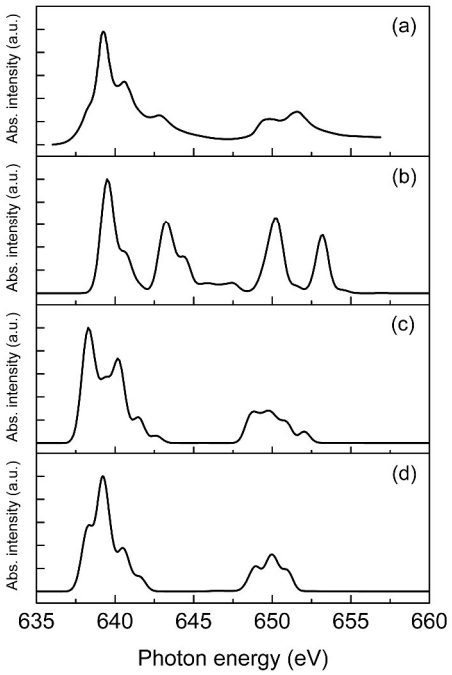

Figure 5. Experimental (a)[42] and simulated $^1L_{2,3}$ XA spectra for different Mn(II) coordinative environments and spin multiplicities: S = 3/2 square planar (b), S = 5/2 square planar (c), S = 5/2 distorted tetrahedral (d). All the simulated spectra have been shifted by 13.4 eV. A 0.8 eV Gaussian broadening has been applied to the energy levels.

To further check this assumption, we have simulated the $^{I}L_{2,3}$-edge XA spectrum for different Mn(II) coordinative environments (distorted tetrahedral and square-planar) and spin multiplicities (S = 5/2 for the distorted tetrahedral coordination; S = 5/2 and S = 3/2 for the square planar one).[64] Results reported in Figure 5(b) clearly indicate that the number, the shape, the position and the relative intensities of the $^{I}L_{2,3}$ XA spectral features obtained by assuming a Mn(II) square planar environment and S = 3/2 completely disagree with the experimental evidence.[42-43] Even though such a disagreement is somewhat relieved when a Mn(II) HS (S = 5/2) square planar arrangement is presumed (see Figure 5(c)), both the overall shape of the $^{I}L_{2,3}$ XA spectrum and the relative intensities of its features poorly reproduce the experimental outcomes.[42-43] In contrast to that, the agreement between experiment and theory is very satisfactory when a HS tetrahedral distorted structure for **I** is considered (see Figure 5 (d)). This allows us to avoid any further analysis of the other cases.

The inspection of Figure 3 and Figure 6 (left panel) clearly indicates that relevant contributions to the $^{I}L_{2,3}$-edge intensity distribution arise from states having either GS (S = 5/2, ΔS = 0) or lower (S = 3/2, ΔS = –1) spin multiplicities. As such, electronic excitations involving states with ΔS = 0 are mainly DOMO → SOMO,[71] while those with ΔS = –1 are mostly DOMO → VMO.[71] In more detail, the lower $^{I}L_3$ *EE* side (< 639 eV) includes only states having the GS spin multiplicity, while states with both S = 5/2 and S = 3/2 contribute to the higher $^{I}L_3$ *EE* side (see Figure 6, left panel). At variance to that, states with S = 5/2 and S = 3/2 contribute to the whole $^{I}L_2$ feature. According to Maganas *et al.*,[4] the analysis of these states has been then extended to their M_S values (Figure 6, right panel). Such a survey pointed out that the ground magnetic sublevels |±5/2> contribute for a 36% to the simulated spectrum, while the participation of the |±3/2> and |±1/2> ones amounts to 40% and 25%, respectively. DFT/ROCIS results allow us to assign the evident shoulder $^{I}\mathbf{L}_3^1$ on the lower *EE* side (638.4 eV) of the experimental and simulated $^{I}L_3$ feature to states mainly involving 2p → HOMO-1 single electron excitations with minor contributions from the 2p → HOMO-2 ones.[72] Similarly to $^{I}\mathbf{L}_3^1$, the intense peak $^{I}\mathbf{L}_3^2$ (639.3 eV, see Figure 6) is, as already stressed, dominated by states with S = 5/2 and it involves 2p → HOMO single electron excitations with tiny contributions from the 2p → HOMO-1 ones. Moving to the analysis of the weaker $^{I}\mathbf{L}_3^3$ peak lying at 640.5 eV, the comparable contribution provided by states with S = 5/2 (52%) and S = 3/2 (43%) has to be underlined before anything else. Moreover, it has to be emphasized that transitions with S = 5/2 have to be associated to 2p → HOMO single electron excitations, while those with S = 3/2 involve the 2p → LUMO+2 single electron excitations.[77] As far as the weakest component ($^{I}\mathbf{L}_3^4$ at 641.7 eV, see Figure 6) of the $^{I}L_3$ feature is concerned, it seems relevant that major contributions come from S = 3/2 (60%) mainly involving one electron excitations toward high lying virtual MOs (2p → LUMO+3/LUMO+4).[77]

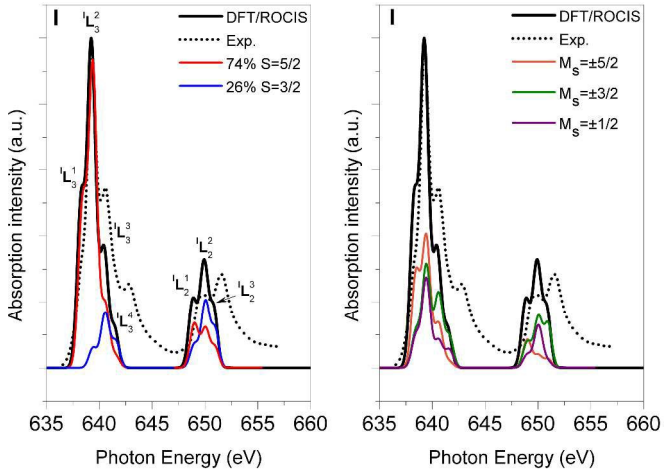

Figure 6. Simulated (black solid line) and experimental (black dotted line)[42] $L_{2,3}$-edge spectrum of **I**. (left panel) Red and blue lines represent deconvolution of the simulated spectrum in terms of states with different spin multiplicity (S). (right panel) Orange, green and violet lines represent deconvolution of the simulated spectrum in terms of states with different M_s. Likewise to the value suggested for similar transition metal complexes, the simulated spectrum has been shifted by 13.4 eV[4] and has a Gaussian broadening of 0.8 eV.

Even though it is well known[4] that main deviations between experiment and theory concern the L_2 region, the DFT/ROCIS $^{I}\mathbf{L}_2^2 - {}^{I}\mathbf{L}_3^2$ Δ*EE* quantitatively reproduces the experimental value (~ 11 eV).[42] Moreover, theoretical results indicate that both S = 5/2 and S = 3/2 states contribute to the $^{I}L_2$ components (S = 5/2, $^{I}\mathbf{L}_2^1$ 59%, $^{I}\mathbf{L}_2^2$ 28%, $^{I}\mathbf{L}_2^3$ 28%; S = 3/2, $^{I}\mathbf{L}_2^1$ 32%, $^{I}\mathbf{L}_2^2$ 47%, $^{I}\mathbf{L}_2^3$ 53%). Any further assignment of the L_2 feature is herein avoided as this *EE* region is not unambiguously determined by experiment.[4]

The thorough description of the frontier orbitals of **I** combined to the use of DFT/ROCIS results makes the assignment of the $^{II}L_{2,3}$-edge spectrum rather straightforward (see Figure 4 and Figure 7). It has been already mentioned that $^{II}L_{2,3}$ features have been firstly recorded by Collison *et al.*[44] without providing any accurate analysis of the experimental evidence. Similarly to the $^{I}L_{2,3}$-edge spectrum, the $^{II}L_{2,3}$-edge intensity distribution arises from states having either GS (S = 3/2, ΔS = 0) or lower (S = 1/2, ΔS = –1) spin multiplicities. Furthermore, electronic excitations involving states with ΔS = 0 are mainly DOMO → SOMO,[71] while those with ΔS = –1 are mostly DOMO → VMO (see Figure 4).[71,77] Likewise to **I**, the analysis of these states has been extended to their M_S values (see Figure 7, right panel), pointing out that the GS magnetic sublevels |±3/2> contribute for 44% to the simulated spectrum, while the participation of the |±1/2> ones amounts to 56%. With specific reference to the $^{II}L_3$ region, the evident $^{II}\mathbf{L}_3^1$ shoulder at 778.3 eV is due to states with the same GS multiplicity and it involves 2p → HOMO-1/HOMO one electron excitations. Analogous considerations hold for the $^{II}\mathbf{L}_3^2$ feature at 779.1 eV, dominated by states with S = 3/2 and involving 2p → HOMO one electron excitations.

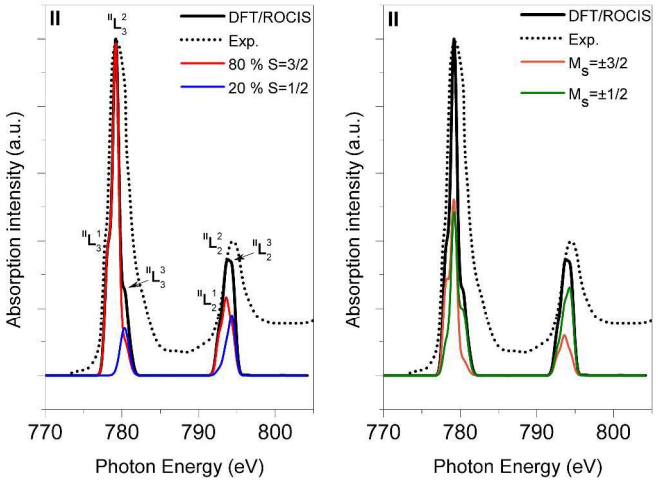

Figure 7. Simulated (black solid line) and experimental (black dotted line)[44] $L_{2,3}$-edge spectrum of **II**. (left panel) Red and blue lines represent deconvolution of the simulated spectrum in terms of states with different spin multiplicity. (right panel) Orange and green lines represent deconvolution of the simulated spectrum in terms of states with different Ms. The simulated spectrum has been shifted by 14.2 eV and has a Gaussian broadening of 0.8 eV.

Interestingly, both S = 3/2 (39%) and S = 1/2 (54%) contribute to the $^{II}L_3^3$ feature (the one lying at the highest *EE* – 780.4 eV). States with S = 3/2 involve 2p → HOMO one electron excitations, while states with S = 1/2 involve DOMO → VMO (2p → LUMO+1, LUMO+2 and LUMO+3) single electron excitations. It is noteworthy that this finding confirms what already underlined in **I** about the participation of states with ΔS = –1 to the higher *EE* side of L_3 (see Figure 6, left panel). Analogously to **I**, the DFT/ROCIS $^{II}L_2^2 - {}^{II}L_3^2$ Δ*EE* quantitatively reproduces the experimental value (~ 15 eV).[44] Furthermore, once again similarly to **I**, theoretical results indicate that both S = 3/2 and S = 1/2 states contribute to the $^{II}L_2$ components (S = 3/2, $^{II}L_2^1$ 83%, $^{II}L_2^2$ 71%, $^{II}L_2^3$ 38%; S = 1/2, $^{II}L_2^1$ 13%, $^{II}L_2^2$ 25%, $^{II}L_2^3$ 50%). Any further assignment of the $^{II}L_2$ feature is herein avoided as this *EE* region is not unambiguously determined by experiment.[4]

4. Conclusions

Literature $L_{2,3}$-edge absorption spectra of $Mn(acac)_2$ and $Co(acac)_2$ have been successfully modeled by using the DFT/ROCIS method. This confirms a distorted tetrahedral coordination around the Mn(II) species. The most intense peak of the $^{I/II}L_{2,3}$-edge spectral patterns ($^{I}L_3^2$ and $^{II}L_3^2$) is dominated by states with the GS spin multiplicity (S = 5/2 in **I** and S = 3/2 in **II**), which involve 2p → HOMO/HOMO-1 single electron excitations. In both complexes, the double degenerate HOMO and HOMO-1 account for an anti-bonding (HOMO) and non-bonding (HOMO-1) interaction with a $(bis\text{-}acac)^{2-}$-based orbital, characterized by the symmetry allowed contribution of both n_-^+, n_-^- and π_3^+, π_3^- pairs. Moreover, the HOMO is significantly localized on the M t_2-like $3d_{xz}/3d_{yz}$ AOs. As such, the participation of the Co-based AOs to the HOMO is lower than the Mn-based ones. Such a result, coupled to the metal contribution in the bonding partner, higher in **II** than in **I**, provides a rationale of the larger overlap population and of the shorter Co–O bond length as compared to the Mn–O bond. As a final consideration, we point out that, similarly to other M(II) complexes characterized by the presence of ligands with low lying empty π* orbitals,[31a,78] the higher *EE* side of both $^{I/II}L_3$ and $^{I/II}L_2$ includes states, which involve metal to ligand charge transfer transitions.

Acknowledgements

Italian Ministry of the University and Research (PRIN-2010BNZ3F2, project DESCARTES), University of Padova (CPDA134272/13, project S_3MArTA), Computational Chemistry Community (C_3P) of the University of Padova are kindly acknowledged.

†In memory of Tom Ziegler passed away on March 24, 2015.

‡Electronic Supplementary Information (ESI) available: Figure S1 contains B3LYP optimized geometries for **I** with a square planar and a distorted tetrahedral arrangement. Tables S1 and S4 include optimized Cartesian coordinated of **I** and **II** with HS tetrahedral structures, respectively; Tables S2-S3 include optimized Cartesian coordinated of **I** with S = 5/2 and S = 3/2, respectively, and imposing a square planar geometry; Tables S5-S6 include selected MOs of **I** and **II**.

References

1 (a) A. Bianconi, in *X-ray Absorption: Principles, Applications, Techniques of EXAFS, SEXAFS and XANES*, D. C. Koningsberger and R. Prins Eds., John Wiley & Sons, New York, 1988, pp. 573–662; (b) J. Stöhr, *NEXAFS Spectroscopy*, Springer, Berlin, 1992.

2 H. H. Zhang, B. Hedman and K. O. Hodgson, *Inorganic Electronic Structure*; E. I. Solomon, A. B. P. Lever; John Wiley & Sons: New York, 1999.

3 E. C. Wasinger, F. M. F. de Groot, B. Hedman, K. O. Hodgson and E. I. Solomon, *J. Am. Chem. Soc.*, 2003, **125**, 12894.

4 D. Maganas, M. Roemelt, T. Weyhermüller, R. Blume, M. Hävecker, A. Knop-Gericke, S. DeBeer, R. Schlögl and F. Neese, *Phys. Chem. Chem. Phys.*, 2014, **16**, 264.

5 D. Maganas, M. Roemelt, M. Hävecker, A. Trunschke, A. Knop-Gericke, R. Schlögl and F. Neese, *Phys. Chem. Chem. Phys.*, 2013, **15**, 7260.

6 G. A. Waychunas, G. E. Brown and M. J. Apted, *Phys. Chem. Miner.*, 1986, **13**, 31.

7 (a) *Metalloproteins: Theory, Calculations, and Experiments*, A. R. Cho and W. A. Goddard III Eds., CRC Press Taylor&Francis Group, FL, 2015; (b) *Practical Approaches to biological Inorganic Chemistry*, R. R. Crichton and R. O. Louro Eds., Elsevier, 2012.

8 The absorption edges are labelled in the order of increasing energy, K, L_1, L_2, L_3, M_1,..., corresponding to the excitation of an electron from the 1s ($S_{1/2}$), 2s ($S_{1/2}$), 2p ($P_{1/2}$), 2p ($P_{3/2}$), 3s (S1/2), ... orbitals (states), respectively.

9 B. E. Douglas and C. A. Hollingsworth, *Symmetry in Bonding and Spectra, an Introduction*; Academic Press, Inc.: Orlando, 1985; pp 256-257.

10 Electric quadrupole transitions involve states of the same parity and they are ~2 orders of magnitude weaker than electric dipole transitions.
11 J. E. Hahn, R. A. Scott, K. O. Hodgson, S. Doniach, S. R. Desjardins, E. I. Solomon, *Chem. Phys. Lett.*, 1982, **88**, 595.
12 The M K-pre-edge is sensitive to 4p-3d mixing on the order of 1%, thus providing a rather accurate estimate of such a mixing.[13]
13 S. DeBeer George, P. Brant, E. I. Solomon, *J. Am. Chem. Soc.*, 2005, **127**, 667.
14 The L_1-edge of the first transition series M is weak and it provides poor spectroscopic information.[15]
15 R. K. Hocking and E. I. Solomon, *Struct. Bond.*, 2012, **142**, 155.
16 C. S. Schnohr and M. C. Ridgway, *X-Ray Absorption Spectroscopy of Semiconductors*, Springer-Verlag, Berlin Heidelberg, 2015.
17 M. Roemelt and F. Neese, *J. Phys. Chem. A*, 2013, **117**, 3069.
18 (a) F. de Groot, *Coord. Chem. Rev.*, 2005, **249**, 31; (b) F. de Groot and A. Kotani, *Core Level Spectroscopy of Solids*, CRC Press, Boca Raton, 2008.
19 (a) P. S. Bagus, H. Freund, H. Kuhlenbeck and E. S. Ilton, *Chem. Phys. Lett.*, 2008, **455**, 331; (b) H. Ikeno, T. Mizoguchi and I. Tanaka, *Phys. Rev. B*, 2011, **83**, 155107; (c) I. Josefsson, K. Kunnus, S. Schreck, A. Föhlisch, F. de Groot, P. Wernet and M. Odelius, *J. Phys. Chem. Lett.*, 2012, **3**, 3565; (d) M. Roemelt, D. Maganas, S. DeBeer and F. Neese, *J. Chem. Phys.*, 2013, **138**, 204101; (e) D. Maganas, S. DeBeer and F. Neese, *Inorg. Chem.*, 2014, **53**, 6374.
20 In the near past, **II** has been the object of great attention as a consequence of its application in controlled radical polymerization processes.[21-23]
21 S. Maria, H. Kaneyoushi, K. Matyjaszewski and R. Poli, *Chem-Eur. J.*, 2007, **13**, 2480.
22 A. Debuigne, J. R. Caille and R. Jerôme, *Angew. Chem. Int. Ed.*, 2005, **44**, 1101.
23 H. Kaneyoshi and K. Matyjaszewski, *Macromolecules*, 2006, **39**, 2757.
24 N. E. Gruhn, L. J. Michelsen and B. L. Westcott, *Inorg. Chem.*, 2002, **41**, 5907.
25 F. A. Cotton, C. E. Rice and G. W. Rice, *Inorg. Chim. Acta*, 1977, **24**, 231.
26 F. A. Cotton and G. W. Rice, *New J. Chem.*, 1977, **1**, 301.
27 Z. Xue, J.-C. Daran, Y. Champouret and R. Poli, *Inorg. Chem.*, 2011, **50**, 11543.
28 (a) G. J. Bullen, *Nature*, 1956, **177**, 537; (b) G. J. Bullen, R. Mason and P. Pauling, *Inorg. Chem*., 1965, **4**, 456.
29 $Ni(acac)_3$ is converted to $Ni(acac)_2$ in coordinating solvents, where an octahedral geometry is formed by coordination of two solvent molecules in *cis* and *trans* forms.[30]
30 (a) Md. Kudrat-E-Zahan, Y. Nishida and H. Sakiyama, *Inorg. Chim. Acta*, 2010, **363**, 168; (b) R. R. Sharp, S. M. Abernathy and L. L. Lohr, *J. Phys. Chem.*, 1997, **107**, 7620; (c) S. M. Abernathy and R. R. Sharp, *J. Phys. Chem. A*, 1997, **101**, 3692.
31 (a) G. Mangione, L. Pandolfo, M. Sambi, G. Ligorio, M. V. Nardi, A. Cossaro, L. Floreano and M. Casarin, *Eur. J. Inorg. Chem*., 2015, 2707; (b) M. Rancan, J. Tessarolo, M. Casarin, P. L. Zanonato, S. Quici and L. Armelao, *Inorg. Chem.*, 2014, **53**, 7276; (c) K. M. Sharples, E. Carter, C. E. Hughes, K. D. M. Harris, J. A. Platts and D. M. Murphy, *Phys. Chem. Chem. Phys.*, 2013, **15**, 15214.
32 J. H. Guo, A. Gupta, P. Sharma, K. V. Rao, M. A. Marcus, C. L. Dong, J. M. O. Guillen, S. M. Butorin, M. Mattesini, P. A. Glans, K. E. Smith, C. L. Chang and R. Ahuja, *J. Phys.: Condens. Matter*, 2007, **19**, 172202.
33 L. Zeng, A. Huegel, E. Helgren, F. Hellman, C. Piamonteze and E. Arenholz, *Appl. Phys. Lett.*, 2008, **92**, 142503.
34 S. Granville, B. J. Ruck, A. R: H. Preston, T. Stewart, F. Budde, H. J. Trodahl, A. Bittar, J. E. Downes and M. Ridgway, *J. Appl. Phys.*, 2008, **104**, 103710.
35 R. Qiao, T. Chin, S. J. Harris, S. Yan and W. Yang, *Curr. Appl. Phys.*, 2013, **13**, 544.
36 V. S. Coker, C. I. Pearce, R: A: D. Pattrick, G. van der Laan, N. D. Telling, J. M. Charnock, E. Arenholz and J. R. Lloyd, *American Mineralogist*, 2008, **93**, 1119.
37 S. Bonhommeau, N. Pontius, S. Cobo, L. Salmon, F. M. F. de Groot, G. Molnar, A. Bousseksou, H. A. Dürr and W. Eberhardt, *Phys. Chem. Chem. Phys.*, 2008, **10**, 5882.
38 M. M. Grush, J. Chen, T. L. Stemmler, S. J. George, C. Y. Ralston, R. T. Stibrany, A. Gelasco, G. Christou, S. M. Gorun, J. E. Penner-Hahn and S. P. Cramer, *J. Am. Chem. Soc.*, 1996, **118**, 65.
39 A. Lussier, J. Dvorak, Y. U. Idzerda, S. B: Ogale, S. R. Shinde, R. J. Choudary and T. Venkatesan, *J. Appl. Phys.*, 2004, **95**, 7190.
40 D. Bazin, I. Kovacs, L. Guczi, P. Parent, C. Laffon, F. de Groot, O. Ducreux and J. Lynch, *J. Catal.*, 2000, **189**, 456.
41 H. Liu, J. Guo, Y. Yin, A. Augustsson, C. Dong, J. Nordgren, C. Chang, P. Alivisator, G. Thornton, D. F. Ogletree, F. G. Requejo, F. De Groot and M. Salmeron, *Nano Lett.*, 2007, **7**, 1919.
42 M. M. Grush, Y. Muramatsu, J. H. Underwood, E. M. Gullikson, D. L. Ederer, R. C. C. Perera and T. A. Callcott, *J. El. Spec. Rel. Phen.*, 1998, **92**, 225.
43 Grush *et at.*[42] compared the $L_{2,3}$-edge XA spectra of $Mn(acac)_2$, $Mn(acac)_3$, MnPc, MnPcCl, MnF_2 and $MnCl_2$ (Pc = phthalocyanine) to look into oxidation states, ligand environment and local structure surrounding the Mn centers.
44 D. Collison, C. D. Garner, C. M. McGrath, J. F. W. Mosselmans, M. D. Roper, J. M. W. Seddon, E. Sinn and N. A. Young, *J. Synchrotron Rad.*, 1999, **6**, 585.
45 F. Neese, *Wiley Interdiscip. Rev.: Comput. Mol. Sci.*, 2012, **2**, 73.
46 Optimized Cartesian coordinates of **I** and **II** are reported in Tables S1-S4 of ESI.
47 (a) A. D. Becke, *Phys. Rev. A*, 1988, **38**, 3098; (b) A. D. Becke, *J. Chem. Phys.*, 1993, **98**, 5648.
48 (a) F. Weigend and R. Ahlrichs, *Phys. Chem. Chem. Phys.*, 2005, **7**, 3297; (b) F. Weigend, *Phys. Chem. Chem. Phys.*, 2006, **8**, 1057.
49 A detailed description of basis sets' acronyms is reported in the ORCA manual (https://orcaforum.cec.mpg.de/).
50 As far as the L_3-edge position is concerned, Maganas *et al.*[4] have shown that the B3LYP/def2-TZVP/J combination provides a very good agreement between theory and experiment, while the functional/basis set combination scarcely affects the overall spectrum shape.
51 (a) E. J. Baerends, D. E. Ellis, and P. Ros, *Chem. Phys.*, 1973, **2**, 41; (b) B. I. Dunlap, J. W. D. Connolly, and J. R. Sabin, *J. Chem. Phys.*, 1979, **71**, 3396; (c) C. Van Alsenoy, *J. Comput. Chem.*, 1988, **9**, 620.
52 D. A. Pantazis, X. Y. Chen, C. R. Landis and F. Neese, *J. Chem. Theory Comput.*, 2008, **4**, 908.
53 V. I. Lebedev, *Zh. Vychisl. Mat. Fiz.*, 1975, **15**, 48.

54 D. Coster and R. D. L. Kronig, *Physica*, 1935, **2**, 13.
55 M. Radon, M. Srebro and E. Broclawik, *J. Chem. Theory Comput.*, 2009, **5**, 1237.
56 P. Pietrzyk, M. Srebro , M. Radon, Z. Sojka and A. Michalak, *J. Phys. Chem. A*, 2011, **115**, 2316.
57 V. D. Vreshch, J. H. Yang, H. Zhang, A. S. Filatov and E. V. Dikarev, *Inorg. Chem.*, 2010, **49**, 8430.
58 J. Burgess, J. Fawcett, D: R. Russell and S. R. Gilani, *Acta Crystallogr.*, 2000, **C56**, 649.
59 F. A. Cotton and R. H. Soderberg, *Inorg. Chem.*, 1964, **3**, 1.
60 F. A. Cotton and R. H. Holm, *J. Am. Chem. Soc.*, 1960, **82**, 2979.
61 (a) A. Debuigne, Y. Champouret, R. Jerôme, R. Poli and C. Detrembleur, *Chem-Eur. J.*, 2008, **14**, 4046; (b) A. Debuigne, C. Michaux, C. Jerôme, R. Jerôme, R. Poli and C. Detrembleur, *Chem-Eur. J.*, 2008, **14**, 7623.
62 $Mn(acac)_3$ has received much more attention in the recent past.[63]
63 (a) F. Neese, *J. Am. Chem. Soc.*, 2006, **128**, 10213; (b) J. Krzystek, G. J. Yeagle, J. H Park, R. D. Britt, M. W. Meisel, L. C. Brunel and J. Telser, *Inorg. Chem.*, 2003, **42**, 4610; (c) B. R. Stults, R. S. Marianelli and V. W. Day, *Inorg. Chem*., 1979, **18**, 1853.
64 Optimized Cartesian coordinates of **I** with tetrahedral (S = 5/2) and square planar arrangements (S = 5/2 and S = 3/2) are reported in Tables S1, S2 and S3 of ESI, respectively.
65 Atomic multiplets associated to the presence of six (eight) electrons in the 3d AOs are: ^5D, ^3H, ^3G, $^3F_{\pm}$, ^3D, $^3P_{\pm}$, ^1I, $^1G_{\pm}$, ^1F, $^1D_{\pm}$, $^1S_{\pm}$ (^3F, ^3P, ^1G, ^1D, ^1S) for a total of 210 (45) microstates.[66] The number of final state pure spin-functions that can be formed from the $2p^53d^6$ and $2p^53d^8$ configurations are 600 and 150, respectively.
66 The interested reader may refer to Table 4.8 of ref. 18b.
67 The $\Delta S = 0$ spin-selection rule is slightly released when SOC is considered. More specifically, SOC connects the terms with resultant spins S and S', where $|S - S'| = 0, 1$.[68]
68 S. Sugano, Y. Tanabe and H. Kamimura, *Multiplets of Transition-Metal Ions in Crystals*, 1970, Academic Press, New York.
69 F. D. Lewis, G. D. Salvi, D. R. Kanis and M. A. Ratner, *Inorg. Chem.,* 1993, **32**, 1251.
70 HOMO and LUMO acronyms stand for highest occupied MO and lowest unoccupied MO, respectively.
71 According to their occupation numbers, MOs are divided in doubly occupied MOs (DOMOs), singly occupied MOs (SOMOs) and virtual (empty) MOs (VMOs).
72 The bonding combination between the M t_2-like *xz*/*yz* AOs and the $n_-^+, n_-^- / \pi_3^+, \pi_3^-$ (bis-acac)$^{2-}$-based hybrid corresponds both in **I** and **II** to the HOMO-6 (see Table S5 and S6 of the ESI).
73 Among the five Co(II) 3d-based AOs, the most stable one is the t_2-like *xy* AO.
74 Any Jahn-Teller distortion[75] is herein neglected.
75 H. A. Jahn and E. Teller, *Proc. R. Soc. London*, 1937, **A161**, 220.
76 R. S. Mulliken, *J. Chem. Phys.* 1955, **23**, 1833.
77 The quasi degenerate LUMO and LUMO+1, both of them of a_2 symmetry, correspond to π_4^+ and π_4^- (π_4^- and π_4^+) ligand-based combinations in **I** (**II**). Any mixing with M-based 3d AOs is forbidden by symmetry. Both the LUMO+2 and the LUMO+3 are of a_1 symmetry; the former is strongly localized on M s AOs, the latter is a ligand based MO accounting for a C–H anti-bonding interaction.
78 G. Mangione, M. Sambi, M. V. Nardi and M. Casarin, *Phys. Chem. Chem. Phys.*, 2014, **16**, 19852.

